

Numerical Study of Flow Noise of an Underwater Vehicle with Different Attack Angles

Bohan Xie¹, Jie Zhu², Yuan Zhuang¹, Decheng Wan^{1*}

¹ Computational Marine Hydrodynamics Lab (CMHL), School of Naval Architecture, Ocean and Civil Engineering, Shanghai Jiao Tong University, Shanghai, China

² Wuhan Second Ship Design and Research Institute, Wuhan, China

*Corresponding Author

ABSTRACT

When the underwater vehicle undergoes pitching motion, an angle of attack is induced, resulting in asymmetric flow characteristics on the upper and lower surfaces of the hull. Although some studies have investigated the effect of the attack angle on the hydrodynamic performances of underwater vehicles, it still remains a gap in research concerning the effect on hydroacoustic characteristics. In this paper, flow field and flow noise of an underwater vehicle at a Reynolds number of 1.2×10^7 with different attack angles ($\alpha=0^\circ$, $\alpha=5^\circ$ and $\alpha=10^\circ$) are numerically simulated using wall-modeled large-eddy simulation (WMLES) and FW-H equation. The current numerical setup is validated with previous studies and shows good consistency. It is found that the attack angle significantly increases the pressure fluctuations at the stern of the hull, and simultaneously increases the radiated noise in almost all directions. When the attack angle is $\alpha=10^\circ$, the radiated noise on the side of the hull is approximately 5dB compared to the case with attack angle $\alpha=0^\circ$.

KEY WORDS: Underwater vehicle; attack angle; large-eddy simulation; pressure fluctuation; flow noise;

INTRODUCTION

Flow noise generated by pressure fluctuation in the turbulent boundary layer is one of the major sources of hydrodynamic noise for underwater vehicles (Wang et al., 2006; Zhao et al., 2022). When the underwater vehicle undergoes pitching, the distribution of pulsating pressure on the hull surface changes due to the attack angles, leading to a variation in the flow noise characteristics. Therefore, exploring the flow noise of underwater vehicles with different motion postures is of vital importance.

Considering the high cost and lengthy period of experimental tests, numerical simulations for underwater vehicles based on computational fluid dynamics (CFD) have become a reasonable alternative (Bhatti et al., 2020). Several high-fidelity simulations have been conducted for underwater vehicles recently, focusing on detailed resolution of

turbulent flow and prediction of noise. Typically, Posa (2016, 2020) and Kumar et al. (2018) extensively discussed the evolution of the boundary layer and the bimodal distribution of turbulent stress in the wake flow of underwater vehicles. Qu et al. (2021) applied the Liutex method to identify the vortex structures of underwater vehicles, and explored the generation mechanisms and evolutionary processes of various vortices. Hu et al. (2023) discussed the errors and the uncertainty in the unsteady turbulent flow around the underwater vehicle. Liu et al. (2023) used 1.476 billion grids to simulate the turbulent flow around the underwater vehicle, and proposed a geometrical-based mesh reordering method to improve cache utilization. Ma et al. (2024) investigated the distributions of dipole and quadrupole noise of an underwater vehicle by impermeable and permeable FW-H methods. Wang et al. (2025) reproduced the unsteady oscillations of the horseshoe vortex at the sail-hull junction flow, and revealed its evolution process.

Since large-eddy simulation (LES) requires a large amount of computational grids to resolve the viscous sublayer of the boundary layer, it becomes computationally expensive to simulate the high Reynolds number flows using LES, such as flow around underwater vehicles (Piomelli, 2008; Choi and Moin, 2012). To address this problem, an improved LES approach for modeling the inner layer while resolving the outer layer of the boundary layer is proposed, which is known as WMLES (Kawai and Larsson, 2012; Bose and Park, 2018). It has been widely proved that WMLES is capable to accurately simulate the mechanical properties and turbulent flow characteristics of underwater vehicles (Chen et al., 2023; He et al., 2023). Furthermore, WMLES also has a reliable performance in predicting the flow noise of underwater vehicles. Wang et al. (2021) studied the hydrodynamic noise of underwater vehicles with different shapes of the sail. Zhou et al. (2022) analyzed the directivity of instantaneous sound pressure caused by the constructive and destructive interference between the lift dipole and the side-force dipole of an underwater vehicle. Jiang et al. (2024) provided the power spectral density (PSD) of the surface pulsating pressure and radiated noise of underwater vehicles using high order numerical scheme. Zhou et al. (2024) numerically simulated the turbulent flow field and hydrodynamic noise of a body of revolution at

a Reynolds number of 1.9×10^6 , and captured the spectral humps near multiples of the blade-passing frequency and accompanying valleys.

However, to the best of our knowledge, previous studies on the flow noise of underwater vehicles have been carried out under the condition of a zero attack angle, without considering the variations in the hydroacoustic characteristics of underwater vehicles in different motion postures. In this paper, turbulent flow structures and flow noise characteristics of underwater vehicles at three different attack angles are simulated with WMLES and FW-H equation. The findings of this study offer valuable insights for enhancing the acoustic stealth performance of underwater vehicles.

NUMERICAL METHODS

Governing Equations

In this paper, WMLES is used to simulate the turbulent flow. Similar to wall-resolved large-eddy simulation (WRLES), WMLES resolve the filtered three-dimensional Navier-Stokes by spatial filtering. The spatial filtered governing equations for incompressible viscous fluid can be expressed as follows (Smagorinsky, 1963):

$$\frac{\partial \bar{u}_i}{\partial x_i} = 0 \quad (1)$$

$$\frac{\partial \bar{u}_i}{\partial t} + \frac{\partial}{\partial x_j} (\bar{u}_i \bar{u}_j) = -\frac{1}{\rho} \frac{\partial \bar{p}}{\partial x_i} + \nu \frac{\partial^2 \bar{u}_i}{\partial x_j^2} - \frac{\partial \tau_{ij}}{\partial x_j} \quad (2)$$

where the subscripts i and j represent streamwise, wall-normal and spanwise directions, the overline symbol represents the spatial filtering, p is the pressure, ν is the kinematic viscosity of fluid, $\tau_{ij} = \bar{u}_i \bar{u}_j - \overline{u_i u_j}$ is the sub-grid stress to describe the interactions between the large-scale eddies and small-scale eddies.

The sub-grid scale model selected in this paper is wall-adapting local eddy-viscosity (WALE) model, which takes both the shear stress tensor and the rotation tensor into account based on the square of the velocity gradient tensor (Nicoud and Ducros, 1999). The expression of sub-grid viscosity ν_t of WALE is as follows:

$$\nu_t = (C_w \Delta)^2 \frac{(S_{ij}^d S_{ij}^d)^{3/2}}{(S_{ij}^d S_{ij}^d)^{5/2} + (S_{ij}^d S_{ij}^d)^{5/4}} \quad (3)$$

where C_w is the model coefficient, Δ is the grid filter width defined by cell volume, S_{ij}^d is the tensor defined as follows:

$$S_{ij}^d = \frac{1}{2} \left(\frac{\partial \bar{u}_i}{\partial x_k} \frac{\partial \bar{u}_k}{\partial x_j} + \frac{\partial \bar{u}_j}{\partial x_k} \frac{\partial \bar{u}_k}{\partial x_i} \right) - \frac{1}{3} \delta_{ij} \frac{\partial \bar{u}_k}{\partial x_k} \frac{\partial \bar{u}_k}{\partial x_k} \quad (4)$$

Wall-stress Model

For WMLES, the wall-stress model is used to describe the velocity distribution in the inner layer of the turbulent boundary layer. In the current simulation, the algebraic model is introduced to approximate the relationship between normalized distance y^+ and normalized velocity u^+ . According to Reichardt (1951), the algebraic wall-stress can be expressed as follows:

$$u^+ = \frac{1}{\kappa} \ln(1 + \kappa y^+) + C(1 - e^{-y^+/y_m^+} - \frac{y^+}{y_m^+} e^{-by^+}) \quad (5)$$

$$C = \frac{1}{\kappa} \ln\left(\frac{E}{f\kappa}\right) \quad (6)$$

$$b = \frac{1}{2} \left(y_m^+ \frac{\kappa}{C} + \frac{1}{y_m^+} \right) \quad (7)$$

where κ is the von Karman constant, E is the log law offset, f is the roughness function, and y_m^+ corresponds to the theoretical intersection of the viscous sub-layer and the log-layer solution. To avoid the log-layer mismatch, the wall shear stress is calculated using the velocity at the second cell away from the wall as reference cell in the current simulation.

Acoustic Model

The FW-H equation, proposed by Ffowcs Williams and Hawkins (1969), is a reliable mathematical model for predicting hydrodynamic noise. Based on the Lighthill's acoustic analogy (Lighthill, 1952; Lighthill, 1954), FW-H equation extends it to the scenario with arbitrary moving rigid boundary in the flow field. The original FW-H equation can be expressed as follows:

$$\left(\frac{1}{c_0^2} \frac{\partial^2}{\partial t^2} - \nabla^2 \right) p' = \frac{\partial}{\partial t} [\rho_0 v_n \delta(f)] - \frac{\partial}{\partial x_i} [p n_i \delta(f)] + \frac{\partial^2}{\partial x_i x_j} [H(f) T_{ij}] \quad (8)$$

$$T_{ij} = \rho u_i u_j - \sigma_{ij} + (p - c_0^2 \rho') \delta_{ij} \quad (9)$$

where p' is the sound pressure, c_0 is the sound speed of the fluid, ρ_0 is the undisturbed density of the fluid, v_n is the wall-normal velocity of the integral surface, n_i is the normal vector to the surface, T_{ij} is the Lighthill stress tensor, $\delta(f)$ is the Dirac function, $H(f)$ is the Heaviside function, σ_{ij} is the viscous stress tensor, δ_{ij} is the Kronecker symbol.

The FW-H equation represents sound sources as monopole, dipole and quadrupole sources, which are associated with the mass fluctuation, pressure fluctuation and turbulent fluctuation of the flow, respectively. Solution of the FW-H equation in integral form is usually obtained by the Farassat 1A formulation (Brentner and Farassat, 1998), in which the monopole and dipole sources are resolved on the sound source surface and the quadrupole source is resolved within the sound source volume. For underwater vehicles, it is generally believed that the dipole source is the main noise source using a stationary sound source surface. Therefore, the radiated noise calculated in the current simulation can be simplified as follows:

$$p'(x, t) = -\frac{1}{4\pi} \frac{\partial}{\partial x_i} \int_S \left[\frac{p n_i}{r_{ret}} \right] dS \quad (10)$$

where r is the distance between the observer and sound source, the subscript ret is the retarded time, S is the sound source surface.

Numerical Setup

In this paper, the bare hull SUBOFF is adopted as the underwater vehicle model, as shown in

Fig. 1. Bare hull SUBOFF is an axisymmetric revolution body composed of a streamlined bow, cylindrical parallel mid-body and tapered stern. The maximum diameter of the mid-body is $D=0.508\text{m}$, and the total length of the hull is $L=8.6D$. The lengths of the bow, mid-

body and stern are $2D$, $4.4D$ and $2.2D$, respectively. The three-dimensional Cartesian coordinate system used in the current simulation is also shown in Fig. 1.

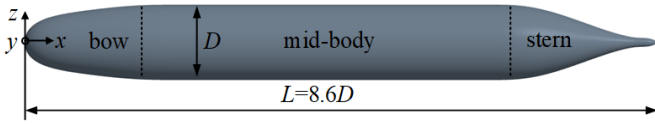


Fig. 1 Geometry of bare hull SUBOFF model

In the current simulation, three cases corresponding to attack angles of $\alpha=0^\circ$, $\alpha=5^\circ$ and $\alpha=10^\circ$ are considered, as shown in Fig. 2. Among them, $\alpha=0^\circ$ is regarded as the base case, where the axis of the hull is aligned with the free-stream direction. Cases $\alpha=5^\circ$ and $\alpha=10^\circ$ are obtained by rotating the hull around the y -axis by 5° and 10° from the case $\alpha=0^\circ$ respectively, with the rotation centered at the hull's center. Apart from the differences in the attack angles, the three cases have the same calculation setup, including the computational domain, computational mesh and numerical schemes. Therefore, the following schematics are presented based on the case $\alpha=0^\circ$.

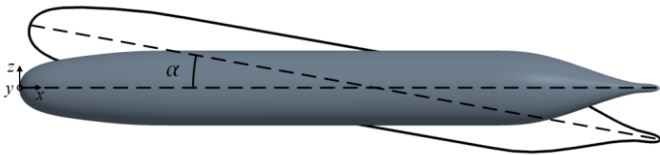


Fig. 2 Schematic of cases with different attack angles α

The computational domain is a rectangular cuboid with dimensions of $38D$ in the streamwise direction, $11D$ in the vertical direction and $11D$ in the spanwise direction, as shown in Fig. 3. The velocity inlet boundary is located $8.5D$ upstream the stagnation point of the hull, while the outlet boundary is positioned $20.9D$ downstream the stern of the hull. The sides of computational domain are set to symmetry planes, and the surface is specified as a no-slip wall. Uniform incoming flow is generated at the inlet boundary with $(U_\infty, 0, 0)$, where U_∞ is the free-stream velocity. The Reynolds number based on L and Mach number based on U_∞ are $Re_L=1.2 \times 10^7$ and $M=2 \times 10^{-3}$.

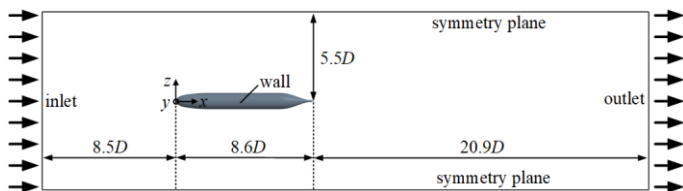


Fig. 3 Schematic of computational domain

Unstructured hexahedral grids are employed to spatially discretize the computational domain, as shown in Fig. 4. A cylindrical region surrounding the SUBOFF model is applied for the mesh refinement, with an isotropic grid size of $1.85 \times 10^{-2}D$, to capture the vortical structures in the flow field. Since resolving the viscous sub-layer of the boundary layer is not required for WMLES, the height of the near-wall grid is set to $1.10 \times 10^{-3}D$, corresponding to $y^+ \approx 30$. At the mid-body region, the aspect ratio of the near-wall grid is approximately 4.2, as shown in the enlarged view in Fig. 4. Besides, 30 prism layers with a

total thickness of $7.09 \times 10^{-2}D$ are added to the SUBOFF surface to ensure a reasonable transition between the near-wall grids and the innermost volumetric grids. The total number of grids is about 73×10^6 .

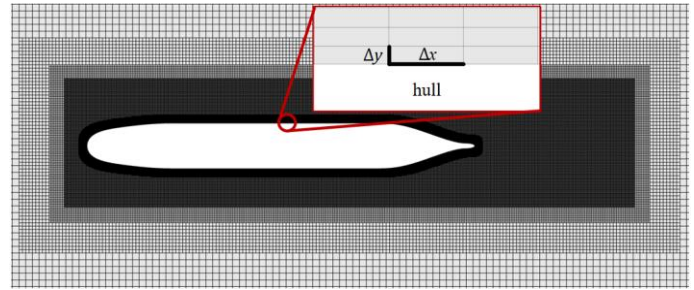


Fig. 4 Schematic of computational mesh on the plane section $y=0$

Before executing WMLES, unsteady RANS with a normalized time-step of $\Delta t_1 U_\infty / D = 0.012$ for a normalized duration of $T_1 U_\infty / D = 60$ is carried out for a fully developed initial flow. Subsequently, the turbulence model is adjusted to WMLES, and the convection scheme is set to bounded-central for high numerical accuracy and stability. The time-step is set to $\Delta t_2 U_\infty / D = 3 \times 10^{-4}$ with the second order temporal discretization, to ensure that the Courant-Friedrichs-Lewy (CFL) number is no more than 0.1. The calculation of WMLES lasts for $T_2 U_\infty / D = 30$, and all the numerical results mentioned below are collected for at least $T_3 U_\infty / D = 6$.

Numerical Validation

In this section, numerical simulation results based on the case $\alpha=0^\circ$ are compared with Kumar et al.'s simulation (2018) and Huang et al.'s experiment (1992), focusing on the pressure coefficient on the hull and the velocity profile at the stern. Pressure coefficient C_p is defined as follows:

$$C_p = \frac{p - p_\infty}{0.5 \rho U_\infty^2} \quad (11)$$

where p_∞ is the free-stream pressure. Distributions of time-averaged C_p along the upper meridian of the hull are shown in Fig. 5. At the bow and stern of the hull, time-averaged C_p value fluctuates due to the influence of the streamwise pressure gradient, while it remains nearly constant around 0 at the mid-body region. Similar magnitudes and evolutions of time-averaged C_p are also reported in previous studies.

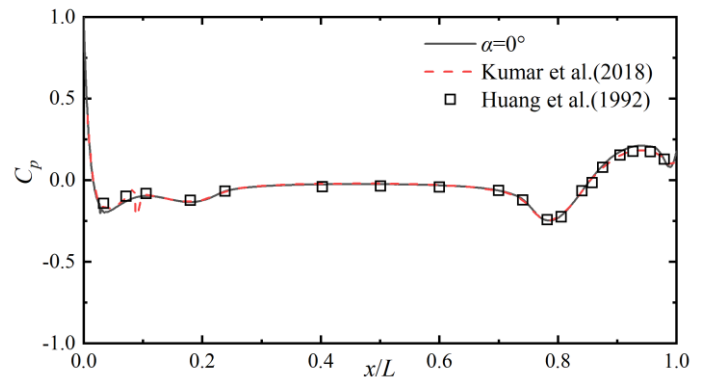


Fig. 5 Distributions of time averaged C_p along the upper meridian of the hull

Normalized time-averaged and root-mean-square streamwise velocity profiles at $x/L=0.904$ are presented in Fig. 6 and Fig. 7, respectively, where r_0 in the vertical coordinate denotes the local radius of the hull. It can be seen that the current simulation has slightly overestimated the time-averaged streamwise velocity by approximately 10% within a distance of $0.2D$ from the hull. However, at greater distance from the hull, the results align well with those from Kumar et al.'s WRLES study. Regarding the root-mean-square streamwise velocity, both the current simulation and Kumar et al.'s WRLES have reported higher values at the near-wall region, compared to Huang et al.'s experiment. It suggests that accurately predicting the near-wall velocity pulsations at high Reynolds numbers using WRLES or WMLES still remains a challenge. However, this issue is not the focus of the present study.

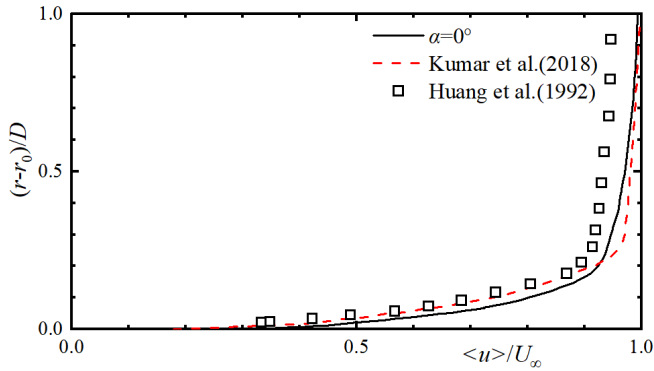


Fig. 6 Normalized time-averaged streamwise velocity profiles at $x/L=0.904$

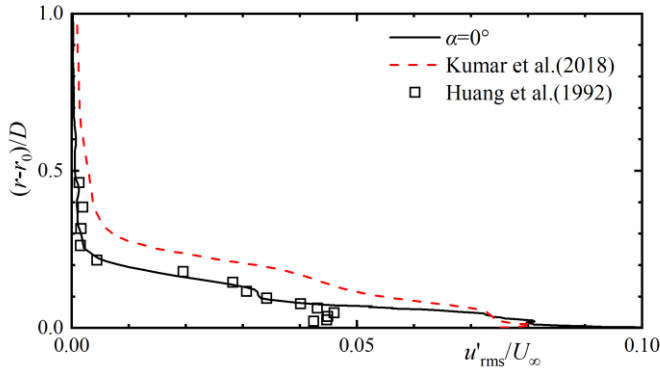


Fig. 7 Normalized root-mean-square streamwise velocity profiles at $x/L=0.904$

In general, the current numerical setup successfully captures the distributions of pressure coefficient and reproduces the velocity profiles at the stern, which validates the accuracy of the numerical methods. Further analysis of the flow field will be discussed in the following section.

RESULTS AND DISCUSSIONS

Normalized instantaneous streamwise velocity on the plane section $y=0$ and time-averaged C_p on the hull with different attack angles are shown

in

Fig. 8. For the case $\alpha=0^\circ$, both the velocity and pressure have exhibited a uniform distribution in the radial direction of the hull. At the mid-body region, the extent of streamwise velocity fluctuations progressively increases, indicating the gradual growth of the turbulent boundary layer thickness. Under the influence of the adverse pressure gradient, the streamwise velocity at the stern of the hull decreases, leading to the formation of a separation vortex. Additionally, with the appearance of the attack angle, the flow exhibits distinct behaviors on the upper and lower surfaces of the hull. On the upper surface, the fluctuations in streamwise velocity are observed over a broader region, particularly at the stern of the hull. In contrast, the fluctuations on the lower surface of the hull are considerably smaller. Besides, with the increase of the attack angle, the pressure on the lower surface at the bow has increased significantly.

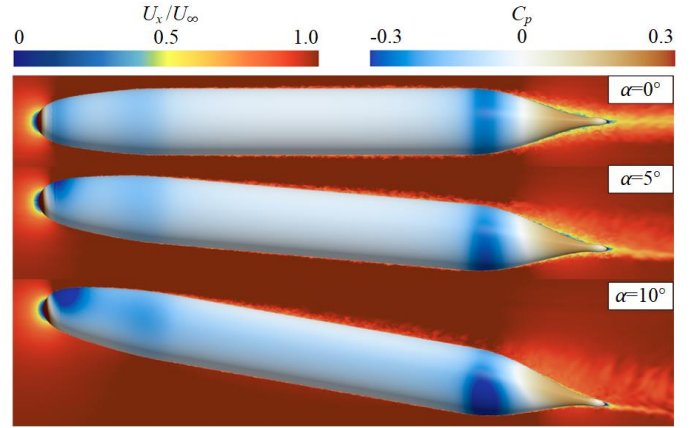


Fig. 8 Normalized instantaneous streamwise velocity on the plane section $y=0$ and time-averaged C_p on the hull with different attack angles

In order to identify the three-dimensional instantaneous turbulent flow structures in the flow field, Q -criterion proposed by Hunt (1988) is introduced in this paper, which can be expressed as follows:

$$Q = \frac{1}{2} (\|\boldsymbol{\Omega}\|^2 - \|\boldsymbol{S}\|^2) \quad (12)$$

where \boldsymbol{S} is the strain rate tensor, $\boldsymbol{\Omega}$ is the rotation rate tensor. Three-dimensional vortical structures around SUBOFF with different attack angles are shown in Fig. 9. Similar to the streamwise velocity evolution, vortical structures are almost evenly distributed on the upper and lower surfaces of the hull for the case $\alpha=0^\circ$. Due to the effect of the attack angle, wall-attached vortices and separation vortices primarily concentrate on the upper surface of the hull. Flow on the lower surface of the hull remains nearly laminar, with significantly fewer vortex formations. It suggests that when the underwater vehicle is inclined upward, the upper surface of the hull may serve as a stronger sound source.

Instantaneous vortical structures at cross-sections $x=0.5L$ (at the mid-body) and $x=0.9L$ (at the stern) with different attack angles are shown in Fig. 10. When the attack angle is 0, the vorticity distribution is very uniform in the radial direction of the hull. The turbulent boundary layer thickens under the adverse pressure gradient at the stern, resulting in a more extensive high-vorticity region at the cross-section $x=0.5L$ compared to the cross-section $x=0.9L$. With the increase of the attack

angle, the high-vorticity region beneath the hull decreases, while the high-vorticity region on both sides of hull become thicker, particularly at the cross-section $x=0.9L$. When the attack angle $\alpha=10^\circ$, vortices shed from the mid-body are observed in the region away from the hull, showing no significant influence on the turbulent boundary layer at the stern.

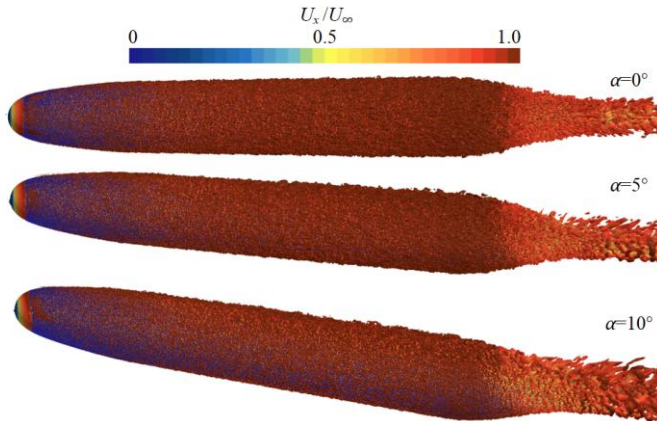


Fig. 9 Instantaneous three-dimensional vortical structures around the SUBOFF with different attack angles identified by the iso-surface $Q \times D^2/U^2=0.3$ colored by normalized instantaneous streamwise velocity

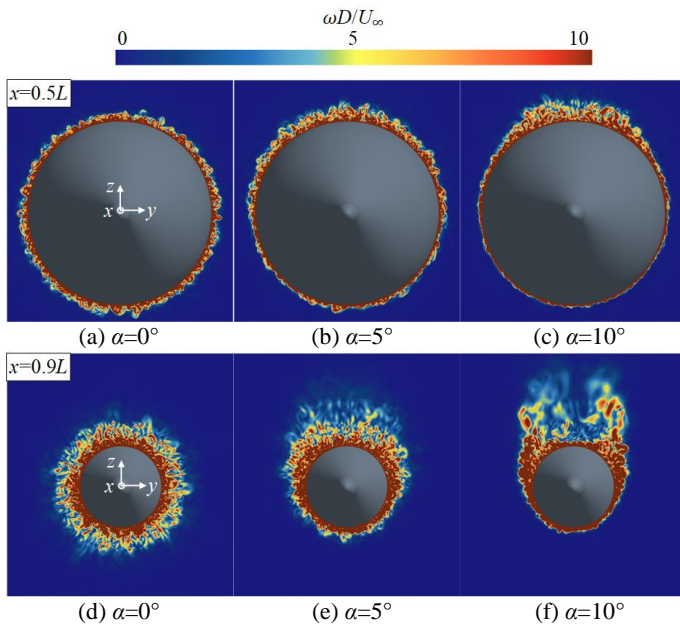


Fig. 10 Instantaneous vortical structures at two typical cross-sections with different attack angles

Several probes are arranged on the surface of the hull to monitor the pressure fluctuation, as shown in Fig. 11. Probes P1, P3, P5, P7 are located on the upper, lower, right and left surfaces of the hull at the mid-body part, respectively. At the corresponding azimuthal positions, probes P2, P4, P6, P8 are positioned at the stern of the hull. When there is an attack angle between the hull and the free-stream, the relative positions of the probes with respect to the hull remain constant.

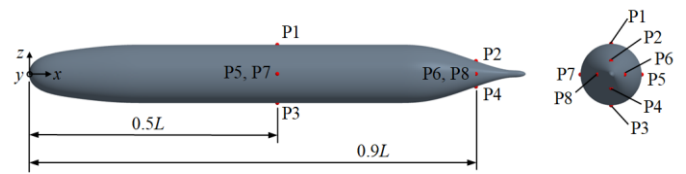


Fig. 11 Schematic of pressure fluctuations probes on the hull PSD of pressure fluctuations normalized by p_{ref} are shown in Fig. 12, where p_{ref} is the reference sound pressure in the water. Frequency of the spectra is nondimensionalized using the Strouhal number $St=fD/U_\infty$. It can be seen that even with an attack angle on the hull, there is no significant variation in the pressure fluctuations at the mid-body across the majority of frequency ranges. Small differences are observed in PSD at probe P1 with $\alpha=0^\circ$ and at probe P3 with $\alpha=10^\circ$, which have higher pressure fluctuation magnitudes at the range of $20 < St < 30$. Since this frequency range exceeds the plateau region of the PSD, it can be inferred that the effect of the attack angle on the pressure fluctuations of the mid-body is limited. Pressure fluctuations at the stern of the hull have relatively obvious differences. When the attack angle $\alpha=10^\circ$, probes P2 and P4 exhibit higher PSD magnitudes in the middle and high frequency range ($St > 10$), while probes P1 and P3 display increased PSD magnitudes in the low frequency range ($St < 10$). It indicates that the impact of the attack angle on the pressure fluctuations of the hull surface is predominantly reflected at the stern. A larger attack angle results in a substantial increase in the pressure fluctuations across all azimuthal positions at the stern of the hull.

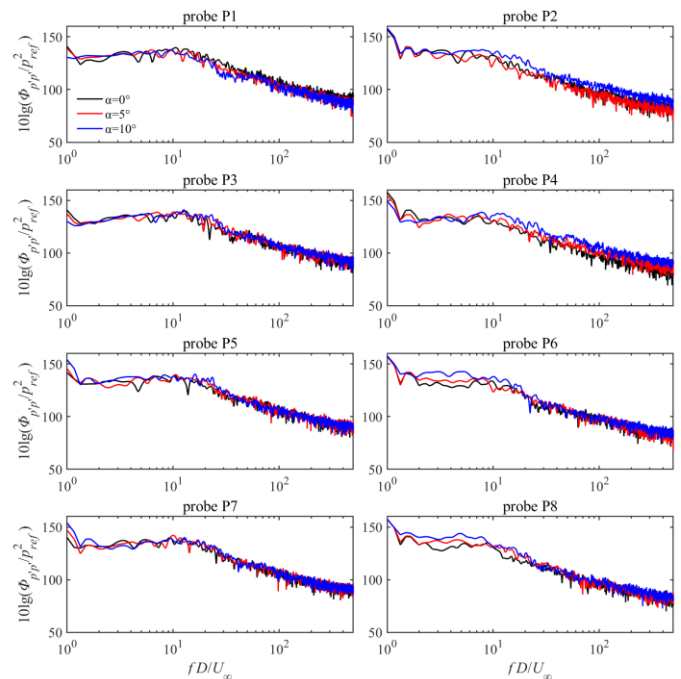


Fig. 12 Normalized PSD spectra of pressure fluctuations with different attack angles

In order to characterize the directivity of radiated noise, 36 noise observers are distributed on the plane sections $x=0.5L$, $y=0$ and $z=0$, respectively. These observers are all positioned $100D$ from the center of the hull, with a 10° interval between adjacent observers. The overall sound pressure level is introduced to describe the magnitude of the radiated noise at each observer, which can be expressed as follows:

$$\text{OASPL} = 10 \lg \left(\sum_N 10^{\frac{\text{SPL}_N}{10}} \right) \quad (13)$$

where N is the number of frequency points within the frequency band, SPL_N is the sound pressure level (SPL) value corresponding to the N th frequency. Directivity of radiated noise with different attack angles on the typical section planes are shown in

Fig. 13. It is observed that the shape of sound directivity has obvious dipole noise characteristics. The radiated noise propagates uniformly in the radial direction of the hull, and noise levels much higher than those in the bow and stern directions of the hull. The most important effect of attack angle on the flow noise is an increase in magnitude across all directions. Furthermore, it can be seen that the sound directivity on the plane section $y=0$ is deflected with the increase of the attack angle. The location of the maximum radiated noise still appears at an angle of approximately 90° relative to the axis of the hull. However, it is noted that the radiated noise above the hull is slightly lower than that at the side of the hull when attack angle is taken into consideration.

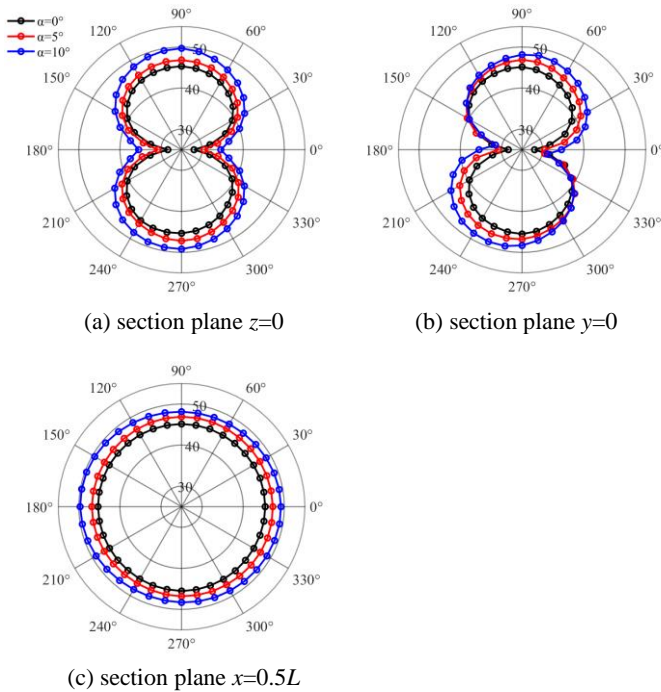


Fig. 13 Directivity of radiated noise with different attack angles

CONCLUSIONS

In this paper, WMLES is applied to simulate the turbulent flow around a bare hull SUBOFF at a Reynolds number of 1.2×10^7 with different attack angles. When the hull has an upward attack angle, the flow on the upper surface of the hull is more intense than the lower surface, including streamwise velocity and vortical structures. It is revealed from the PSD of the surface pressure fluctuations that the attack angle significantly enhances the magnitudes of pressure fluctuations at the stern of the hull. Finally, FW-H equation is adopted to predict the sound directivity at the far-field of the SUBOFF with different attack angles. With the increase of the attack angle, the magnitude of the radiated noise increases significantly in almost every direction. Moreover, the symmetry axis of sound directivity is deflected on the plane section perpendicular to the rotation axis of the attack angle, with the maximum radiated noise observed on the lateral side of the hull.

The current numerical simulation provides valuable data support for the flow field characteristics and hydroacoustic characteristics of the underwater vehicle with pitching motion. The present study focuses on the hydrodynamic noise performance of the underwater vehicle at specific attack angles. Future work will further investigate the hydroacoustic characteristics of underwater vehicles considering multi-degree-of-freedom motion.

ACKNOWLEDGEMENTS

This work is supported by the National Natural Science Foundation of China (52131102), to which the authors are most grateful.

REFERENCES

- Bhatti, MM, Marin, M, Zeeshan, A, and Abdelsalam, SI (2020). "Editorial: Recent Trends in Computational Fluid Dynamics," *Front Phys*, 8, 593111.
- Bose, ST, and Park, GI (2018). "Wall-Modeled Large-Eddy Simulation for Complex Turbulent Flows," *Annu Rev Fluid Mech*, 50(1), 535-561.
- Brentner, KS, and Farassat, F (1998). "Analytical Comparison of the Acoustic Analogy and Kirchhoff Formulation for Moving Surfaces," *AIAA Journal*, 36(8), 1379-1386.
- Chen, S, Yang, L, Zhao, W, and Wan, D (2023). "Wall-modeled large eddy simulation for the flows around an axisymmetric body of revolution," *J Hydrodyn*, 35(2), 199-209.
- Choi, H, and Moin, P (2012). "Grid-point requirements for large eddy simulation: Chapman's estimates revisited," *Physics of Fluids*, 24(1), 011702.
- He, K, Zhou, F, Zhao, W, Wang, J, and Wan, D (2023). "Numerical analysis of turbulent fluctuations around an axisymmetric body of revolution based on wall-modeled large eddy simulations," *J Hydrodyn*, 35(6), 1041-1051.
- Hu, Y, Wu, Q, Zhang, H, Huang, B, and Wang, G (2023). "Verification and validation for large eddy simulation of the turbulent flow around an underwater entity," *Physics of Fluids*, 35(12), 125128.
- Hunt, JCR, Wray, AA, Moin, P (1988). "Eddies, Streams, and Convergence Zones in Turbulent Flows.," *Proceedings of the Summer Program*.
- Jiang, P, Liao, S, and Xie, B (2024). "Large-eddy simulation of flow noise from turbulent flows past an axisymmetric hull using high-order schemes," *Ocean Engineering*, 312, 119150.
- Kawai, S, and Larsson, J (2012). "Wall-modeling in large eddy simulation: Length scales, grid resolution, and accuracy," *Physics of Fluids*, 24(1), 015105.
- Kumar, P, and Mahesh, K (2018). "Large-eddy simulation of flow over an axisymmetric body of revolution," *J Fluid Mech*, 853, 537-563.
- Lighthill (1952). "On sound generated aerodynamically I. General theory," *Proceedings of the Royal Society of London. Series A. Mathematical and Physical Sciences*, 211(1107), 564-587.
- Lighthill (1954). "On sound generated aerodynamically II. Turbulence as a source of sound," *Proceedings of the Royal Society of London. Series A. Mathematical and Physical Sciences*, 222(1148), 1-32.
- Liu, Y, Wang, H, Wang, S, and He, G (2023). "A cache-efficient reordering method for unstructured meshes with applications to wall-resolved large-eddy simulations," *Journal of Computational Physics*, 480, 112009.
- Ma, Z, Li, P, Wang, L, Lu, J, and Yang, Y (2024). "Mechanistic study of noise source and propagation characteristics of flow noise of a submarine," *Ocean Engineering*, 302, 117667.
- Nicoud, F, and Ducros, F (1999). "Subgrid-Scale Stress Modelling Based on the Square of the Velocity Gradient Tensor," *Flow, Turbulence and Combustion*, 62(3), 183-200.

- Piomelli, U (2008). "Wall-layer models for large-eddy simulations," *Progress in Aerospace Sciences*, 44(6), 437-446.
- Posa, A, and Balaras, E (2016). "A numerical investigation of the wake of an axisymmetric body with appendages," *J Fluid Mech*, 792, 470-498.
- Posa, A, and Balaras, E (2020). "A numerical investigation about the effects of Reynolds number on the flow around an appended axisymmetric body of revolution," *J Fluid Mech*, 884, A41.
- Qu, Y, Wu, Q, Zhao, X, Huang, B, Fu, X, and Wang, G (2021). "Numerical investigation of flow structures around the DARPA SUBOFF model," *Ocean Engineering*, 239, 109866.
- Reichardt, H (1951). "Vollständige Darstellung der turbulenten Geschwindigkeitsverteilung in glatten Leitungen," *Z Angew Math Mech*, 31(7), 208-219.
- Smagorinsky, J (1963). "General circulation experiments with the primitive equations: I. The basic experiment," *Mon Wea Rev*, 91(3), 99-164.
- Wang, G, Liu, Y, Wang, S, and He, G (2025). "Assessment of the Reynolds-stress model-based hybrid RANS/LES method for junction flow around a fully appended underwater vehicle," *Ocean Engineering*, 318, 120073.
- Wang, M, Freund, JB, and Lele, SK (2006). "Computational Prediction of Flow-Generated Sound," *Annu Rev Fluid Mech*, 38(1), 483-512.
- Wang, X, Huang, Q, and Pan, G (2021). "Numerical research on the influence of sail leading edge shapes on the hydrodynamic noise of a submarine," *Applied Ocean Research*, 117, 102935.
- Williams, JEF, and Hawkings, DL (1969). "Sound Generation by Turbulence and Surfaces in Arbitrary Motion," *Philosophical Transactions of the Royal Society of London Series A, Mathematical and Physical Sciences*, 264(1151), 321-342.
- Zhao, W, Pan, Z, Yu, L, and Wan, D (2022). "An overview of flow field computational methods for hydrodynamic noise prediction," *J Hydrodyn*, 34(6), 994-1005.
- Zhou, D, Wang, K, and Wang, M (2024). "Rotor aeroacoustic response to an axisymmetric turbulent boundary layer," *J Fluid Mech*, 981, A25.
- Zhou, Z, Xu, Z, Wang, S, and He, G (2022). "Wall-modeled large-eddy simulation of noise generated by turbulence around an appended axisymmetric body of revolution," *J Hydrodyn*, 34(4), 533-554.